Available online at www.sciencedirect.com
ScienceDirect
International Journal of Heat and Fluid Flow 27 (2006) 1010–1027
International Journal of HEAT AND FLUID FLOW
www.elsevier.com/locate/ijhff

Open channel turbulent flow over hemispherical ribs

M. Agelinchaab, M.F. Tachie *

Department of Mechanical and Manufacturing, University of Manitoba, Winnipeg, Manitoba, Canada R3T 5V6

Received 4 October 2005; received in revised form 20 December 2005; accepted 6 March 2006
Available online 3 May 2006

Abstract

This paper reports an experimental investigation of open channel turbulent flow over hemispherical ribs. A row of ribs consists of hemispheres closely placed to one another in the spanwise direction and cover the entire span of the channel. The pitch-to-height ratio is varied to achieve the so-called *d*-type, intermediate and *k*-type roughness. The Reynolds numbers based on water depth, h, and momentum thickness, θ, of the approach flow are respectively, $Re_h = 28{,}100$ and $Re_\theta = 1800$. A particle image velocimetry is used to obtain detailed velocity measurements in and above the cavity. Streamlines, mean velocity and time-averaged turbulent statistics are used to study the effects of pitch-to-height ratio on the flow characteristics and also to document similarities and differences between the present work and prior studies over two-dimensional transverse rods. It was observed that interaction between the outer flow and the shear layers generated by ribs is strongest for *k*-type and least for *d*-type ribs. The results also show that hemispherical ribs are less effective in augmenting flow resistance compared to two-dimensional transverse ribs. The levels of the Reynolds stresses and budget terms increase with increasing pitch-to-height ratio inside the roughness sublayer.

Keywords: Open channel flow; Hemispherical ribs; Wall roughness; Particle image velocimetry

1. Introduction

Turbulent flows over rough surfaces occur in many fluid engineering systems. One effect of surface roughness is to increase momentum transfer and flow resistance. In the area of heat transfer, surfaces are often artificially roughened to augment heat transfer rates. Because of their technological importance, turbulent flow over rough surfaces has been studied quite extensively since the early work of Nikuradse (1933). Different roughness elements such as sand grains, gravels, spheres, wire mesh, and two-dimensional transverse rods attached to surfaces have been used in the past to model surface roughness. The results obtained from prior studies have broadened our knowledge of the structure of rough wall turbulent flow.

Prior research has shown differences between the structure of turbulent flow over smooth and rough surfaces close to the wall or roughness elements. The region over which these differences exist is often referred to as the roughness sublayer, and is defined as the region extending from the wall to about 5 roughness heights (Raupach et al., 1991). Following the terminology of Perry et al. (1969), surface roughness can be classified as *d*-type and *k*-type roughness. If the roughness function depends on Reynolds number based on the roughness height, k, and friction velocity, U_τ, (i.e., $k^+ = kU_\tau/\nu$, where ν is the kinematic viscosity), it is termed *k*-type roughness. Research has shown that the *k*-type scaling is not obeyed by grooved surfaces when the cavities are narrow. This type of roughness scales with outer variables (the boundary layer thickness, δ or the pipe diameter, d) and is therefore known as *d*-type. For flow over ribs made of repeated two-dimensional transverse rods, roughness classification is based on pitch (p) to height (k) ratio, p/k. In this case, *d*-type roughness is obtained if $p/k < 4$, $p/k = 4$ is often referred to as intermediate roughness, and $p/k > 4$ corresponds to *k*-type roughness. In *d*-type and intermediate roughness regime, stable

* Corresponding author. Tel.: +1 204 474 9589; fax: +1 204 275 7507.
E-mail address: tachiemf@cc.umanitoba.ca (M.F. Tachie).

0142-727X/$ - see front matter © 2006 Elsevier Inc. All rights reserved.
doi:10.1016/j.ijheatfluidflow.2006.03.001

Nomenclature

C_f	skin friction coefficient
D	diameter of hemisphere
F_u, F_v	flatness factor of streamwise and wall normal fluctuating velocities
h	water depth
H	boundary layer shape parameter
k	rib (hemisphere) height
k_s	sand grain roughness
p	pitch or distance between crests of adjacent ribs (see Fig. 2)
Re_h	Reynolds number based on freestream velocity and water depth
Re_θ	Reynolds number based on freestream velocity and momentum thickness
S_u, S_v	skewness factor of streamwise and wall normal fluctuating velocities
U	streamwise component of mean velocity
U_e	freestream velocity
U_τ	friction velocity
u, v	fluctuating velocity components in streamwise and wall-normal directions
u^2, v^2	Reynolds normal stress in streamwise and wall-normal directions
$-\langle uv \rangle$	Reynolds shear stress
u^3, u^2v, uv^2, v^3	triple correlations
V_k, V_{uv}	transport velocity for turbulent kinetic energy and Reynolds shear stress
x, y, z	streamwise, wall-normal and spanwise coordinates

Greeks

ε	dissipation rate of turbulent kinetic energy
δ	boundary layer thickness
κ	von Karman constant
Ω_z	mean spanwise vorticity
ν	kinematic viscosity
θ	boundary layer momentum thickness
ΔU^+	roughness shift

Subscript and superscript

$()^+$	normalization by inner variables U_τ and ν
$()_C$, $()_L$, $()_R$	mean velocity or turbulent quantity obtained at cavity center, crest of left (upstream) rib, crest of right (downstream) rib
$()_S$	mean velocity or turbulent quantity obtained by averaging over a pitch

vortices are formed in the cavity between ribs and these vortices prevent the outer flow from reattaching on the floor of the cavity. For k-type roughness, on the other hand, the vortices occupy only a fraction of the cavity and the separated flow may re-attach on the floor.

As mentioned earlier, the velocity and thermal fields of turbulent flow over two-dimensional transverse rods and other roughness geometries have been studied extensively using both experimental and numerical methodologies (Akinlade et al., 2004; Furuya et al., 1976; Grass et al., 1993; Krogstad et al., 1992; Ligrani and Moffat, 1986; Liou et al., 1990; Mazouz et al., 1998; Tachie et al., 2003). Reviews of previous works on rough wall turbulent flow are also provided by Raupach et al. (1991), and more recently by Jiménez (2004). Because it is impractical to review all prior studies, only selected and representative experimental and numerical works over two-dimensional rods are summarized. Djenidi et al. (1999) used a laser Doppler anemometry (LDA) to investigate turbulent boundary layer over two-dimensional square rods. The pitch-to-height ratio was $p/k = 2$ giving a d-type roughness. They observed significant variation of the mean and fluctuating velocity inside the cavity and higher turbulence intensities and Reynolds shear stress over the ribs than for a smooth surface. They also performed qualitative flow visualization using a laser-induced fluorescence to elucidate the importance of outflows in producing and sustaining turbulence. Okomato et al. (1993) studied boundary layer flow over square rods over a wide range of pitch-to-height ratios: $2 \leqslant p/k \leqslant 17$. Their flow visualization revealed stable recirculation for $p/k \leqslant 5$. For $p/k = 9$ they observed that the flow reattached to the floor of the cavity. The turbulence intensity in the shear layer increased for $p/k \leqslant 9$ and decreased for $p/k > 9$, and they concluded that interaction between ribs reached a maximum at $p/k = 9$. Sato et al. (1989) conducted LDA measurements in a channel with both top and bottom walls roughened with 10 mm square rods at $p/k = 7$. The top and bottom rods were arranged in symmetric, staggered and unsymmetric configurations. Detailed velocity measurements at various x-positions between the ribs revealed differences among the different configurations.

Because turbulent flow over ribs is remarkably inhomogeneous inside the cavity and the roughness sublayer, the use of single point velocity measurement techniques such as hot-wires and Pitot tubes may miss some of the salient features close to the ribs. Furthermore, Pitot tube and hot-wires are not ideal for measurements inside the cavity where reverse flow and high local turbulence intensities exist. These limitations are overcome with the use of direct numerical simulation (DNS) and large eddy simulation (LES). Though limited to relatively low Reynolds numbers, the quality and scope of information obtained from LES and DNS are unmatchable by experimental methodologies. Some of the prior numerical works are now reviewed. Cui et al. (2003) performed LES in a channel with the bottom wall roughed with square rods arranged to yield three pitch-to-height ratios, $p/k = 1$, 4, 9, corresponding to

d-type, intermediate and k-type roughness, respectively. The streamlines for the d-type and intermediate roughness show stable vortices occupying the entire cavity. For the k-type roughness, a total of four recirculation regions were observed on the crest and inside the cavity. The outer flow also reattached on the floor in the cavity. Their results show that the interaction between the outer flow and the flow inside the cavity is greatest for k-type and least for d-type roughness.

Miyake et al. (2001), Ikeda and Durbin (2002) and Nagano et al. (2003) performed DNS in channels with one-side of channel roughened by two-dimensional transverse square rods. Leonardi et al. (2003, 2005) also performed DNS in a channel with the bottom wall roughened by two-dimensional square rods for $1 \leqslant p/k \leqslant 19$. Their results also revealed recirculation regions inside the cavity with the outer flow re-attaching on the floor for $p/k \geqslant 7$. They found that the maximum form drag occurs at $p/k = 7$. DNS of channel flow with both bottom and top walls roughened by two-dimensional transverse square rods were performed by Alireza et al. (2004) and Krogstad et al. (2005). The pitch-to-height ratio in both studies was $p/k = 8$ and the rods were arranged in a non-staggered fashion. They noted differences between the rib flow and smooth flow inside the roughness sublayer. However, the streamlines obtained by Alireza et al. (2004) revealed a saddle point close to the floor in the cavity flow rather than the reattachment observed in the work of Leonardi et al. (2003) and Cui et al. (2003).

In this work, a particle image velocimetry (PIV) is used to study open channel turbulent flow over and inside hemispherical ribs. The pitch-to-height ratio was varied to obtain d-type, intermediate and k-type roughness. The rib geometry studied in this work is quite different from the two-dimensional transverse square and circular rods studied in most of the previous studies. Since the PIV is a whole-field velocity measurement technique, it is particularly suitable for studying the remarkably inhomogeneous velocity field inside the cavity and in the immediate vicinity of the ribs.

2. Experimental setup and measurement procedure

2.1. Test facility

The experiments were performed in an open channel recirculation type water channel. The channel is constructed using Plexiglas to facilitate optical access. To ensure smooth entrance of flow into the test section, the settling chamber upstream of the contraction is fitted with perforated steel plates. A 6:1 contraction ratio is used to further reduce the turbulence intensity by accelerating the mean flow. The test section of the channel is 2500 mm long, 200 mm wide and 200 mm deep. The flow is driven by 25HP motor and in-line centrifugal pump system. A Toshiba transistor inverter type variable speed controller regulates the motor-pump system speed. The system is furnished with a filter that removes dye concentrations and other unwanted particles from the working fluid when the need arises.

The ribs were glued on to a 4-mm thick Plexiglas sheet that spans the entire width and length of channel using a double-sided tape. The sheet was then tightly screwed onto the bottom wall of the channel. A row of ribs consists of transparent acrylic hemispheres closely placed to one another in the spanwise direction and cover the entire span of the channel. The ribs were positioned such that the crest of center rib in each row is located in the middle plane of the channel. The average diameter D and height k of the hemispheres provided by the supplier (ComPlex Plastics Inc.) were $D = 12$ mm and $k = 6$ mm. A digital vernier caliper was used to measure the diameters and heights of 30 randomly selected hemispheres. It was found that $12.03 \leqslant D$ (mm) $\leqslant 12.73$ and $5.69 \leqslant k$ (mm) $\leqslant 5.89$. The measured mean diameter D_m and standard deviation σ_D for the diameters were $D_m = 12.23$ mm and $\sigma_D = 0.17$ mm, and corresponding values for the height were $k_m = 5.82$ mm and $\sigma_k = 0.04$ mm. Three different values of pitch, p, or crest-to-crest spacing between successive rows were chosen to achieve d-type, intermediate and k-type roughness. Specifically, values of $p = 12$, 24 and 48 mm were chosen for d-type ($p/k = 2$), intermediate ($p/k = 4$) and k-type ($p/k = 8$) roughness. A 40-mm wide strip of 1-mm sand grains spanning the width of the channel was placed 100 mm from the entrance of the channel to enhance a rapid development of the boundary layer. A schematic of the test section, coordinate system as well as the CCD camera and laser arrangement is shown in Fig. 1. Here, the streamwise, wall-normal and the spanwise directions are denoted by x, y and z, respectively; $x = 0$ corresponds to the upstream edge of the first row of hemispheres, $y = 0$ corresponds to the floor of the channel (Plexiglas sheet), and $z = 0$ corresponds to the middle plane of the channel. The mean and fluctuating velocities will be denoted by upper and lower cases, respectively. For example, U is the mean velocity in the streamwise direction, u and v are the fluctuating components in the streamwise and wall-normal directions, respectively, and $-\langle uv \rangle$ is the Reynolds shear stress in the x–y plane. Fig. 2 shows sketches and pictures of the three roughness types studied. It should be noted that, unlike square rods, the base of the hemispheres for our d-type roughness touches each other. Because the laser was shot from above (Fig. 1), it was necessary to spray the ribs in regions where measurements were taken using a black spray (Krylon Fusion) so as to minimize reflected light from the ribs and improve the quality of vectors close to the ribs.

2.2. PIV system and measurement procedure

The flow was seeded with polyamide seeding particles having mean diameters of 5 μm and specific gravity of 1.03. The settling velocity and response time of the particles were estimated to be 0.41 μm/s and 1.43 μs, respectively.

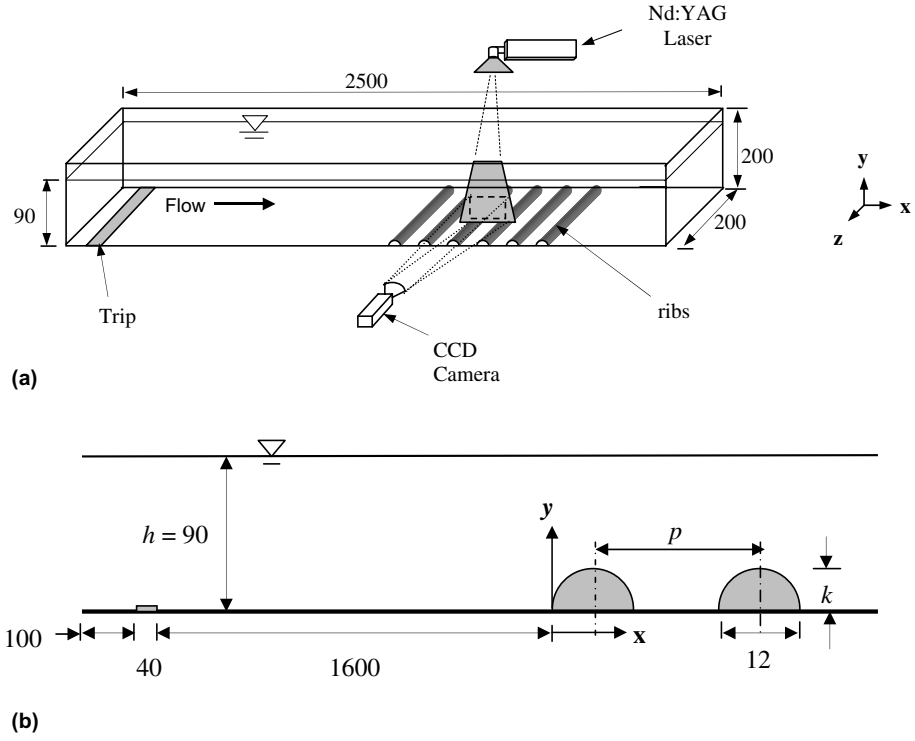

Fig. 1. A schematic of experimental setup showing the test section and coordinate system. All distances are in mm.

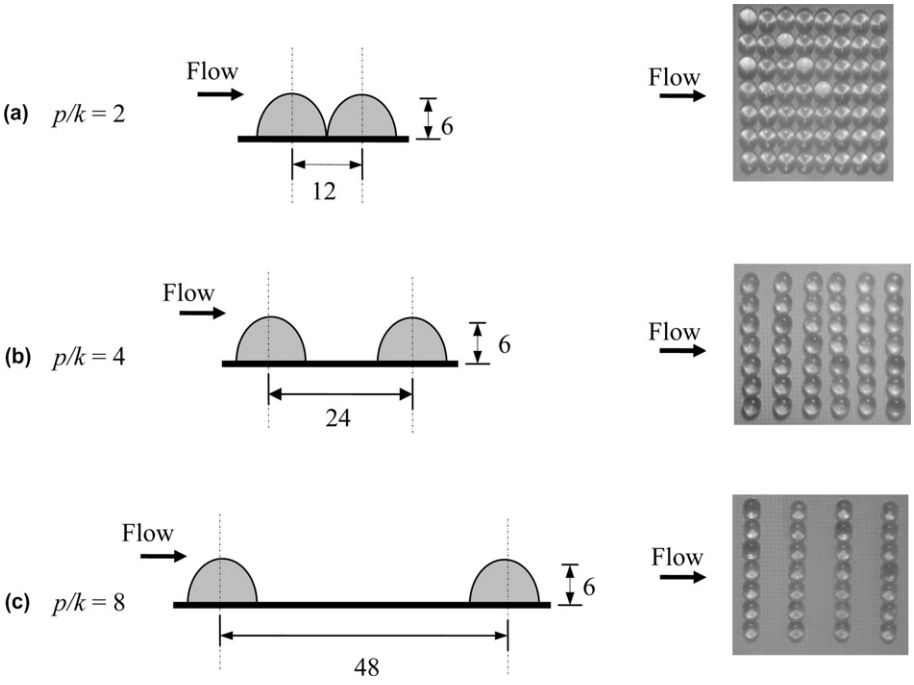

Fig. 2. Sketches and pictures of the roughness types studied: (a) *d*-type, $p/k = 2$; (b) intermediate, $p/k = 4$; (c) *k*-type, $p/k = 8$. All distances are in mm.

The settling velocity is small compared to the mean axial velocity measured and the response is very small compared to the sampling time of about 500 μs so that the particles are considered to follow the fluid faithfully. An Nd-YAG, 120 mJ pulse laser ($\lambda = 532$ nm) was used to illuminate the flow. A set of cylindrical lens converted the laser light into a thin sheet. As shown in Fig. 1, the laser was shot from the top and through the free surface. Since the Froude number ($Fr = U_e^2/gh = 0.14$) is low and the flow is in the sub-critical range, there were no waves. That is, the free surface was nearly parallel and fairly calm and did not distort the laser sheet significantly. The laser sheet was located at the mid-plane ($z = 0$) of the channel and positioned in such a way that its plane was perpendicular

to the camera. A 60 mm diameter Nikkor lens was fitted to a high resolution digital camera (Dantec Dynamic HiSense 4M camera) which uses charged-coupled device (CCD) with 2048 pixel × 2048 pixel chip and a pitch of 7.4 μm. The PIV images were acquired continuously through a buffer system onto a desktop computer. The digital images were post-processed by the adaptive-correlation option of commercial software developed by Dantec Dynamics (FlowManger 4.50.17). Each image was subdivided into 32 pixel × 32 pixel with 50% overlap. Approximately, 20 particles could be found in each interrogation area of the PIV.

Initial measurements were made upstream and over the ribs using a 100 mm × 100 mm field of view. It was determined that the boundary layer thickness δ defined as the y-location where $U = 0.99U_e$ (U_e is the freestream velocity) was 55 mm. Based on this result all subsequent measurements were made with approximately 60 mm × 60 mm field of view giving 0.45 mm × 0.45 mm interrogation area. Preliminary measurements were made to study flow

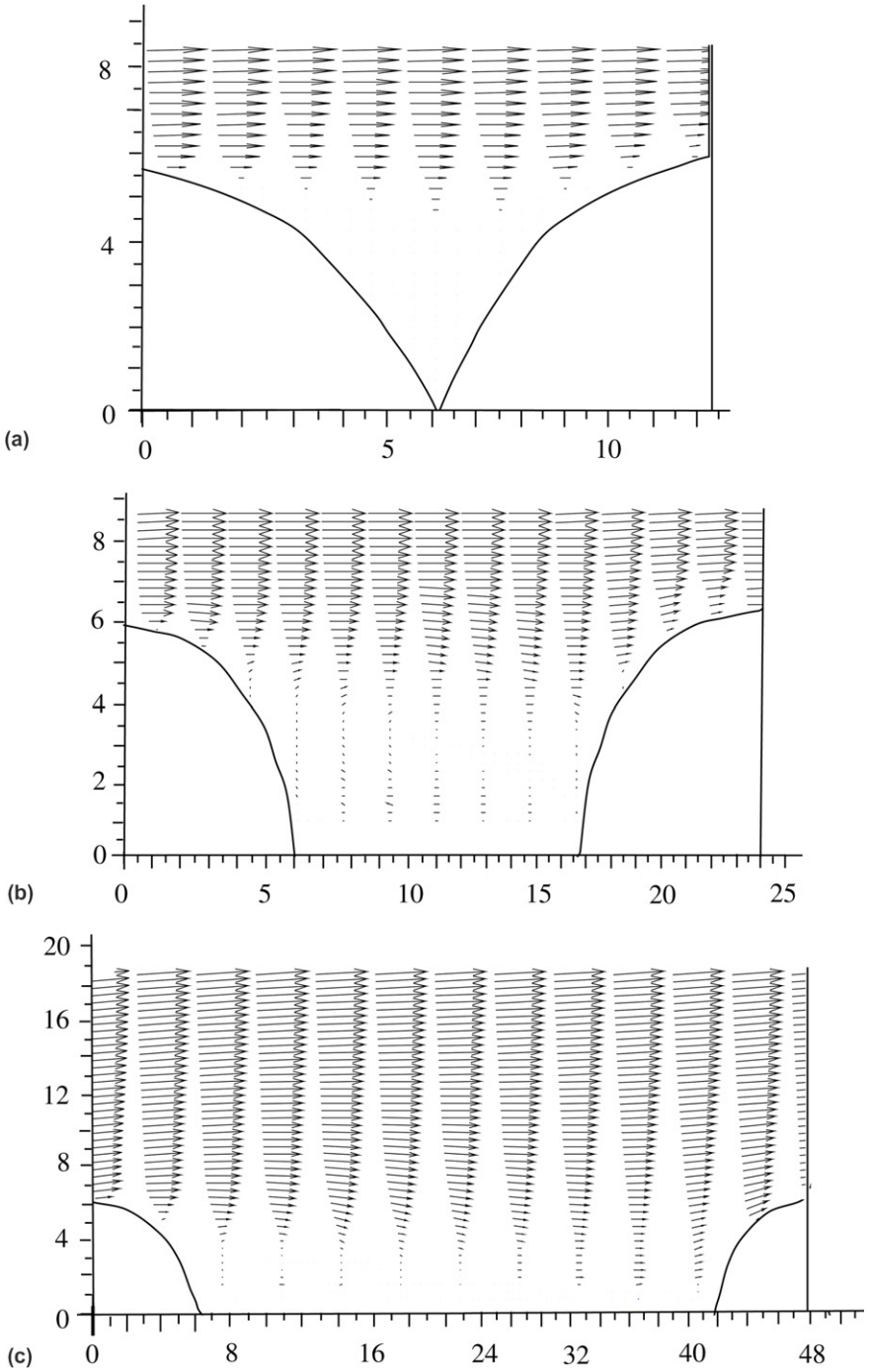

Fig. 3. Velocity vectors inside and above cavity: (a) *d*-type; (b) intermediate; (c) *k*-type. All distances are mm.

development over the ribs. From these results, it was decided to conduct all subsequent measurements beyond the 8th row of hemispheres, i.e., $x/p > 7$. Preliminary analysis was also performed using various sample sizes to compute the mean and the turbulence quantities. It was found that the mean and turbulent profiles obtained using 2000 or more images do not show any significant difference and so 2500 images were used to compute the mean and turbulent statistics reported in this paper. Measurements were made 350 mm upstream of the first row of ribs ($x = -350$ mm) in order to obtain the characteristics of the approach turbulent boundary layer. The mean and turbulent quantities obtained at this location will be referred to as 'smooth' in Section 3. The pertinent boundary layer parameters for the approach flow are as follows: water depth $h = 90$ mm, free stream velocity $U_e = 0.312$ m/s, boundary layer thickness $\delta = 55$ mm, momentum thickness $\theta = 5.79$ mm, shape parameter $H = 1.46$, Reynolds number based on the momentum thickness $Re_\theta = U_e\theta/\nu = 1800$. The background turbulence level measured at $y = \delta$ was approximately 5%.

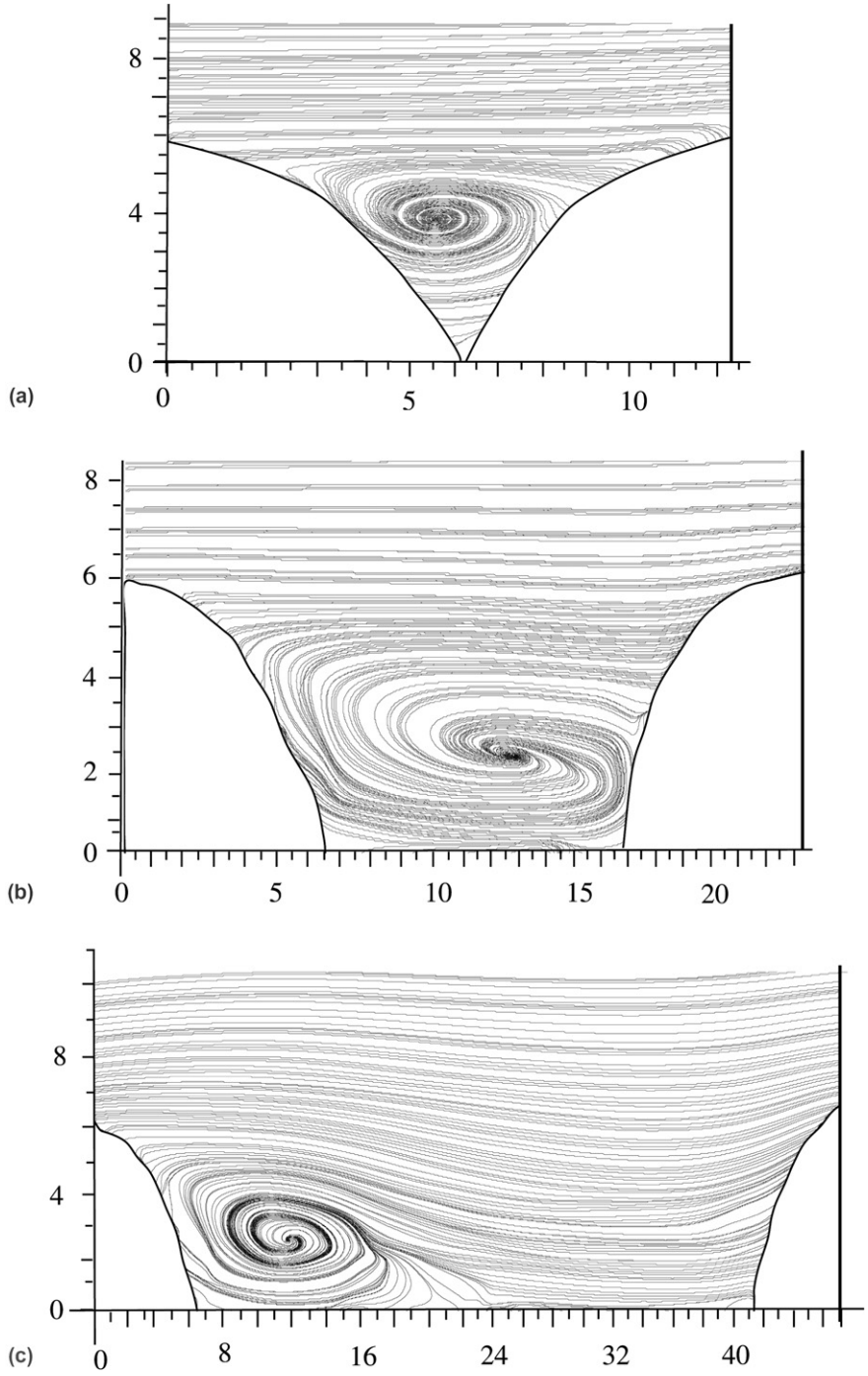

Fig. 4. Streamlines inside and above cavity: (a) *d*-type; (b) intermediate; (c) *k*-type. All distances are in mm.

3. Results and discussion

3.1. Streamlines, mean spanwise vorticity and velocity field in the cavity

Fig. 3 shows velocity vectors inside and above the cavities to reveal how the mean velocity varies along the flow (x-direction) in this region. In each case, some vectors were skipped to avoid data congestion. Since the hemispheres were closely placed (they actually touch each other) for d-type roughness (Fig. 3(a)), there is only a small cavity close to the crests of the hemispheres. The velocity magnitude in the cavities is ordinarily small, and as expected, the vectors vary quite significantly inside the cavities. Negative velocities were found in the cavities revealing flow reversal. The magnitude of the negative velocities in d-type roughness is, however, so small that they are not visible in the figure. It is observed that the mean velocity increases very rapidly above

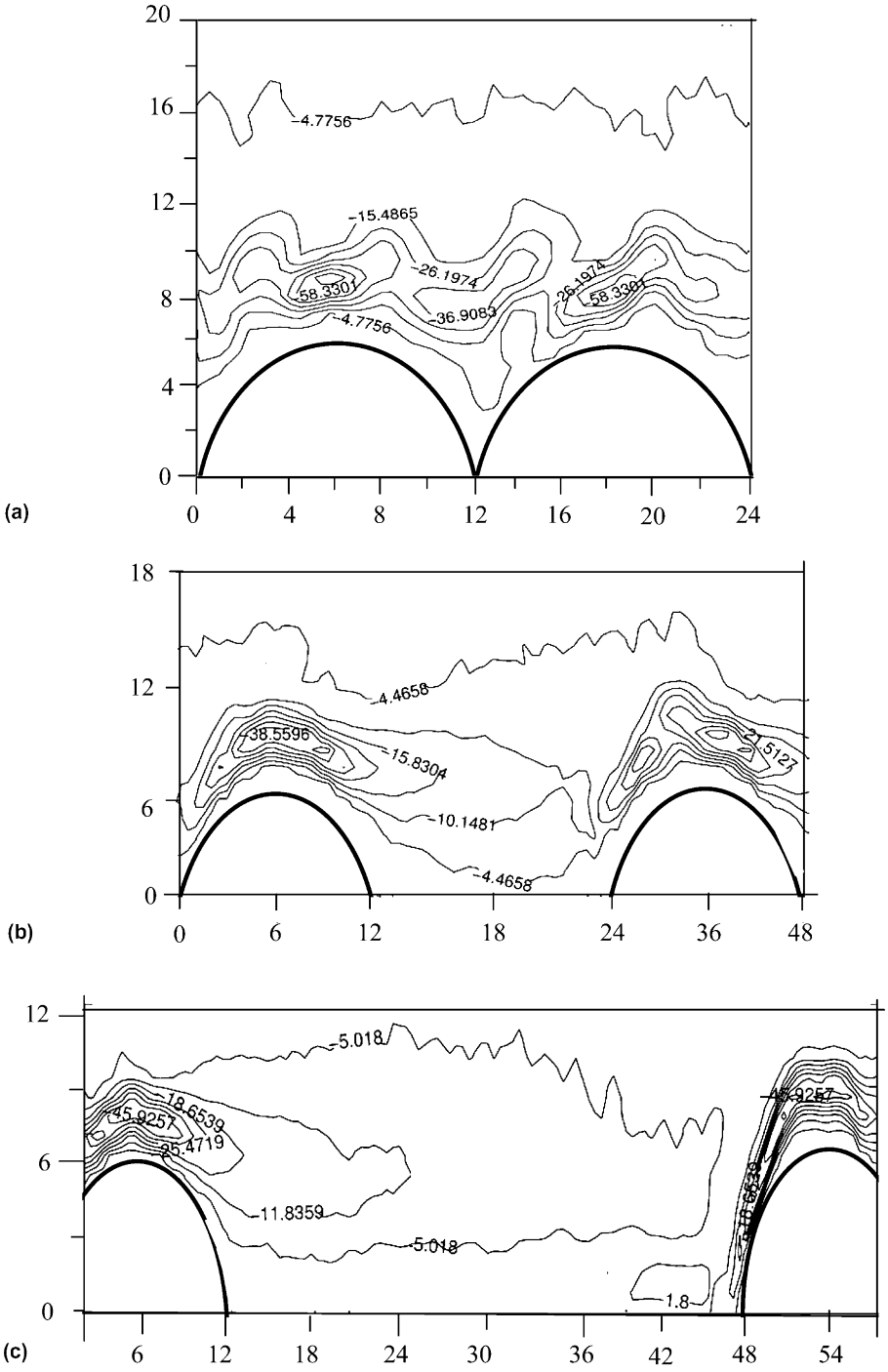

Fig. 5. Isocontours of mean spanwise vorticity inside and above cavity: (a) d-type; (b) intermediate; (c) k-type.

the cavity. The vectors obtained over *d*-type and intermediate roughness are parallel to the main flow just above ribs. However, the mean flow over *k*-type roughness is remarkably inhomogeneous so that the vectors remain unparallel up to $y \approx 18$ mm, i.e., 2 rib heights above the crest.

The streamlines for the three roughness types are shown in Fig. 4. For *d*-type and intermediate roughness, streamlines that originate from the upstream rib reattach on the downstream rib, and not on the floor inside the cavity. For each of these two roughness types, a weak stable clockwise rotating vortex occupies the region bounded by these streamlines and the cavity. The vortex for intermediate roughness is obviously larger than that for *d*-type. Thus, the flow patterns over *d*-type and intermediate hemispherical ribs are qualitatively similar to those obtained in prior numerical results for two-dimensional square ribs except for the corner counter rotating vortex. For *k*-type roughness, the separating streamline from the upstream rib reattaches onto the floor in the cavity at about $4k$ downstream from the crest of upstream rib. In this case too, the space bounded by the separating streamline, the upstream hemisphere and the floor is occupied by a vortex. The size of this vortex is smaller than those obtained for intermediate and *d*-type roughness. Consistent with observation made in Fig. 3(c), the streamlines close to the ribs are not parallel due to a stronger interaction between the outer flow and cavity for *k*-type roughness. It should be noted that our *k*-type roughness does not reveal a distinct counter rotating vortex behind the upstream rib. Further, the smaller vortices found on the crest and just upstream

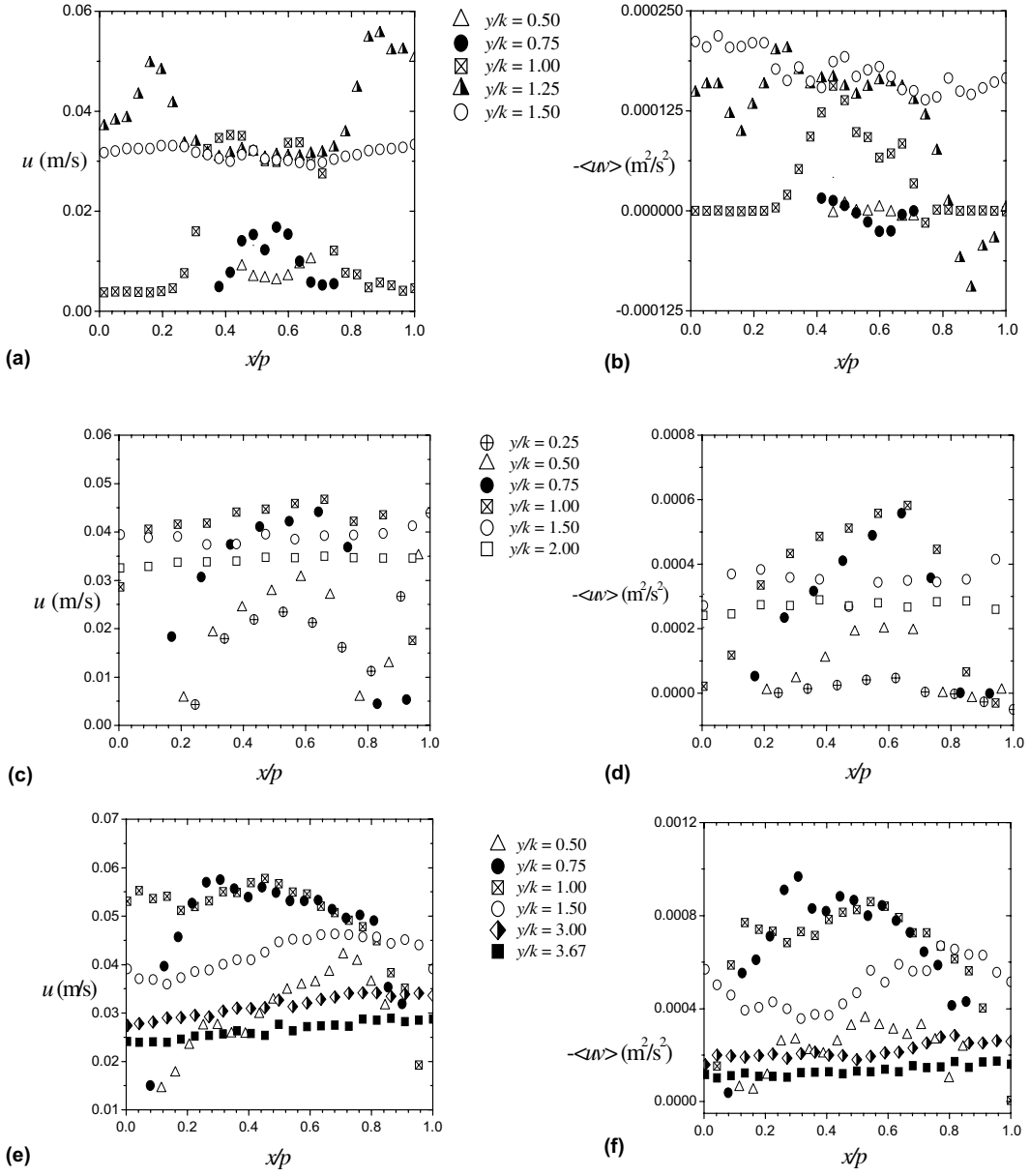

Fig. 6. Variation of turbulence intensity (u) in the streamwise direction and Reynolds shear stress $-\langle uv \rangle$ with x at selected y-locations inside the cavity and above the ribs. (a) and (b) *d*-type; (c) and (d) intermediate; (e) and (f) *k*-type.

of the downstream rod in the LES results of Cui et al. (2003) over square rods were not observed in the present work. The separating bubble for our k-type ribs is shallower than reported for square rods. These disparities are probably due to differences in rib geometry. The observation that the flow reattaches onto the floor in the k-type cavity is consistent with the DNS results of Leonardi et al. (2003) and LES results of Cui et al. (2003) in a channel with one wall roughened but at variance with Alireza et al. (2004) whose DNS results pertain to a channel with both walls roughened with square rods.

The isocontours of mean spanwise vorticity ($\Omega_z = \partial V/\partial x - \partial U/\partial y$) are shown in Fig. 5. The figure reveals regions of intense shear layer in the vicinity of the ribs. Because $\partial V/\partial x < \partial U/\partial y$, values of Ω_z are negative everywhere. The bulk of vorticity is generated above the ribs and convected downstream into the cavity. Inside the cavity, more intense vorticity is found for d-type ribs than for intermediate and k-type ribs. As noted above, a reduced interaction between the outer flow and d-type cavity produces negligible vertical motion ($V \approx 0$) inside the d-type cavity. In this case, the mean vorticity simplifies to $\Omega_z \approx -\partial U/\partial y$.

The variation of turbulence intensity (u) in the streamwise direction and the Reynolds shear stress $-\langle uv\rangle$ with x at selected y-locations inside the cavity and above the ribs are shown in Fig. 6. For d-type roughness, the u profiles are nearly symmetrical with two peaks located upstream and downstream of the vortex centre. The maximum value occurred at $y/k = 1.25$, i.e., above the ribs. The Reynolds shear stress also show double peak but the upstream peak is higher than the downstream peak. For intermediate roughness, the maximum values of u and $-\langle uv\rangle$ occur at $y/k = 1.00$ and $x/p = 0.65$. Further, both u and $-\langle uv\rangle$ profiles are nearly parallel for $y/k \geqslant 2.0$. In the case of the k-type roughness, u and $-\langle uv\rangle$ do not become homogeneous until $y/k = 3.67$. The locations of maximum u and $-\langle uv\rangle$ occur at $y/k = 0.75$ mm and $x/p = 0.4$, that is, below the top plane of the ribs and upstream of the reattachment. In summary, Fig. 6 clearly demonstrates that locations of the maximum u and $-\langle uv\rangle$ move closer to the floor as the pitch-to-height ratio increases.

3.2. Mean velocity profiles in outer and inner coordinates

Because of the significant variation of the mean and turbulent quantities in the cavity and above the ribs (for k-type), it was decided to average the mean and turbulent

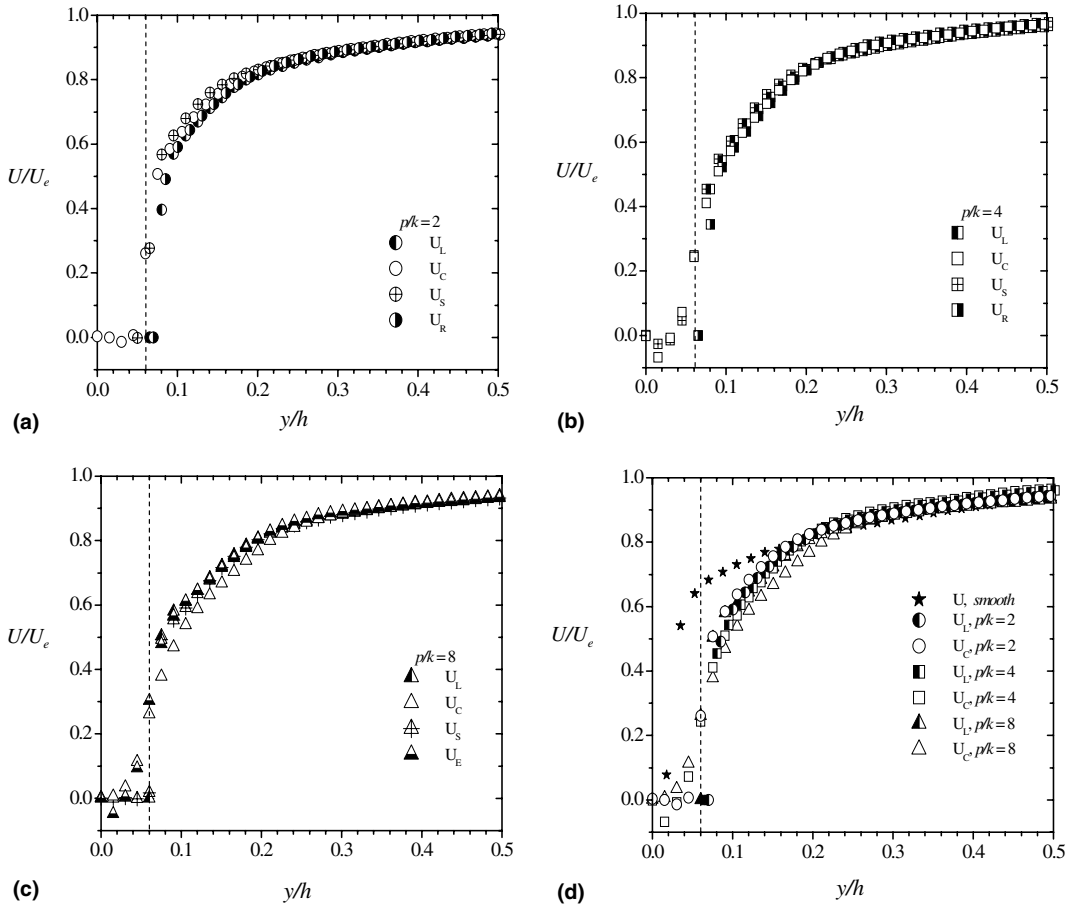

Fig. 7. Mean velocity profiles normalized by freestream velocity (a) d-type, (b) intermediate, (c) k-type and (d) comparison among smooth and various roughness types.

quantities over a wavelength p, i.e., from crest to crest, and compare these profiles with those obtained at the crest and cavity center. In subsequent figures, the subscripts R and L will be used to denote profiles obtained at the crests of the right (downstream) and left (upstream) ribs, respectively, and C will denote profiles at centre of cavity. For example, U_R, U_L and U_C will denote U profiles obtained at crest of the downstream rib, crest of the upstream rib and centre of cavity respectively. Similarly, U_S will denote averaging over a wavelength, p, i.e., from upstream crest to downstream crest. Note that because the flow over k-type roughness reattaches on the floor, the vortex center is not located at the cavity center. For this reason, profiles were also extracted at x-location corresponding to the vortex center for k-type roughness. These profiles will be denoted by the subscript E so that U_E, for example, will denote the mean velocity at vortex centre of k-type roughness.

The mean velocity profiles are shown in Fig. 7. The velocity, U, and wall-normal distance relative to the floor, y, are normalized by the free stream velocity, U_e, and the water depth, h, respectively. The profiles are terminated at $y/h = 0.5$ (or $y/k = 7.5$) because data beyond this point do not provide any valuable information. The dash lines correspond to the top plane of the ribs. Profiles at cavity centre are negative for d-type and intermediate roughness because these locations correspond to the vortex centre. For k-type roughness, U_E profile shows negative values but U_C does not because the x-location of the former corresponds to the vortex center while for the latter, it is located downstream of reattachment. The magnitude of maximum negative velocity is about 10% of freestream velocity for the intermediate roughness but lower for d-type and k-type roughness. Fig. 7(a) and (b) show that, for d-type and intermediate roughness, the various profiles including the spatial-averaged profiles, collapsed reasonably well in the region $y/h > 0.1$. The data also reveal that profiles at adjacent crests (U_L and U_R) are nearly indistinguishable right from the rib top. For k-type roughness

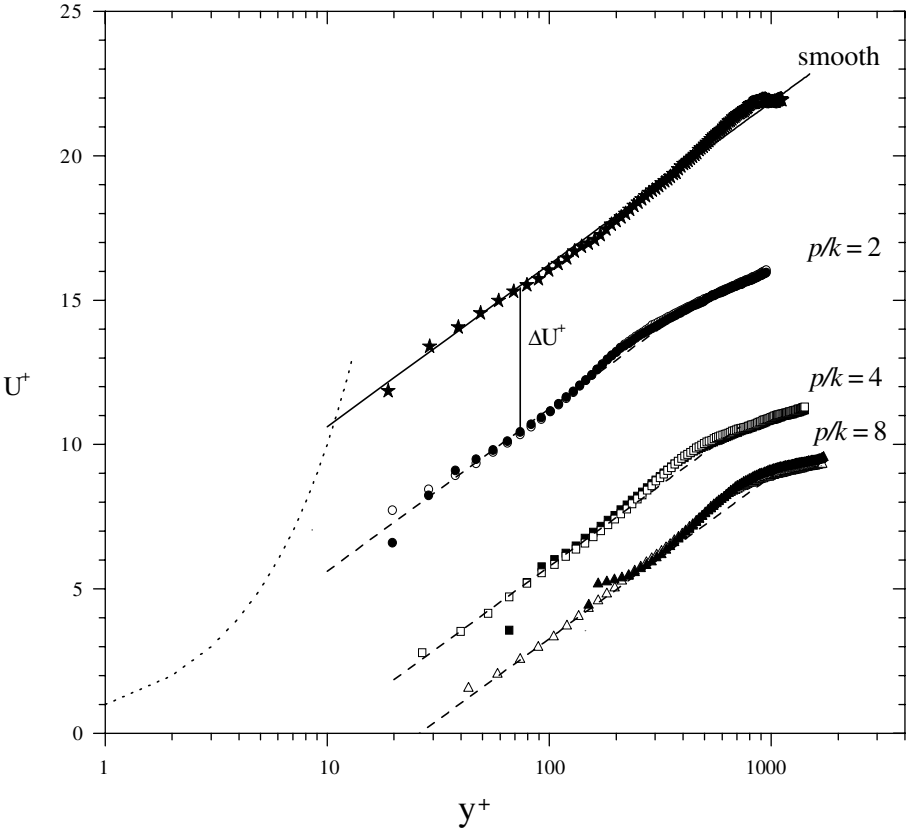

Fig. 8. Mean velocity profiles in inner coordinates.

Table 1
Summary of friction and roughness parameters from averaged velocity profiles for the various surface conditions studied

Surface type	U_e (m/s)	U_τ (m/s)	U_τ/U_e	C_f	ΔU^+	k_s^+	k_s/k
Smooth	0.312	0.0143	0.046	0.0042	–	–	–
d-type ($p/k = 2$)	0.325	0.020	0.062	0.0076	5.00	32.6	0.27
Intermediate ($p/k = 4$)	0.325	0.029	0.089	0.0159	10.45	304.8	1.75
k-type ($p/k = 8$)	0.325	0.034	0.105	0.0219	12.95	849.5	4.16

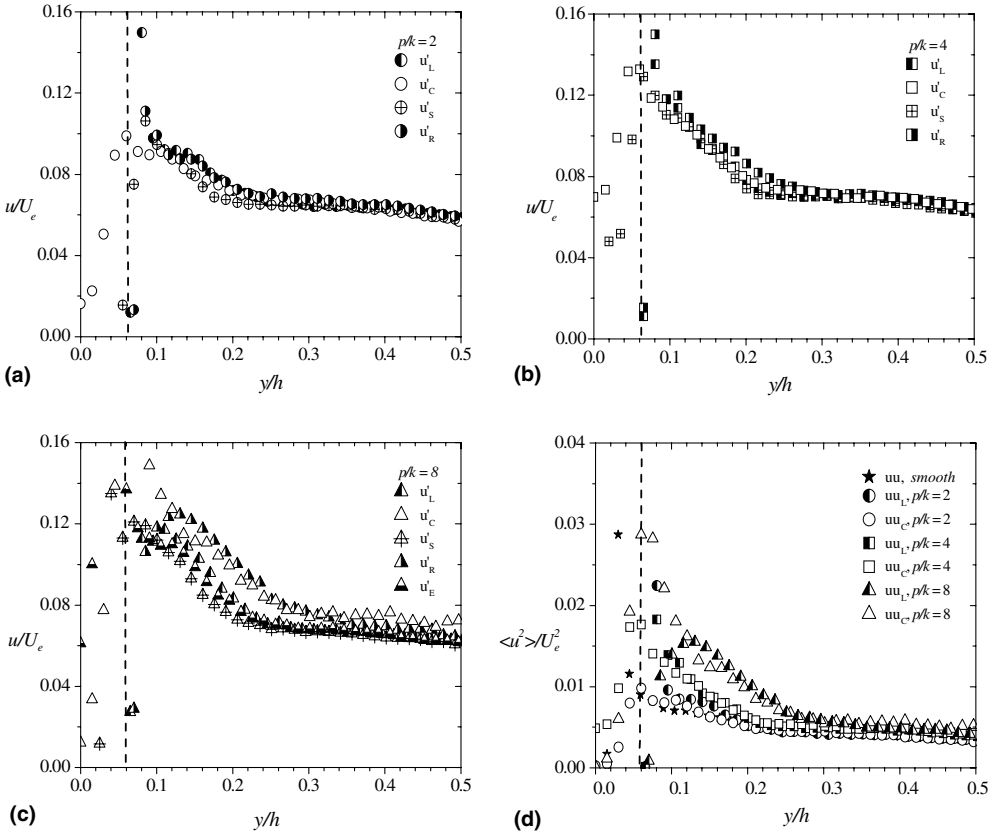

Fig. 9. Streamwise turbulent intensity (u) and Reynolds stress ($\langle u^2 \rangle$) normalized by freestream velocity (a) d-type, (b) intermediate, (c) k-type and (d) comparison among smooth and various roughness types.

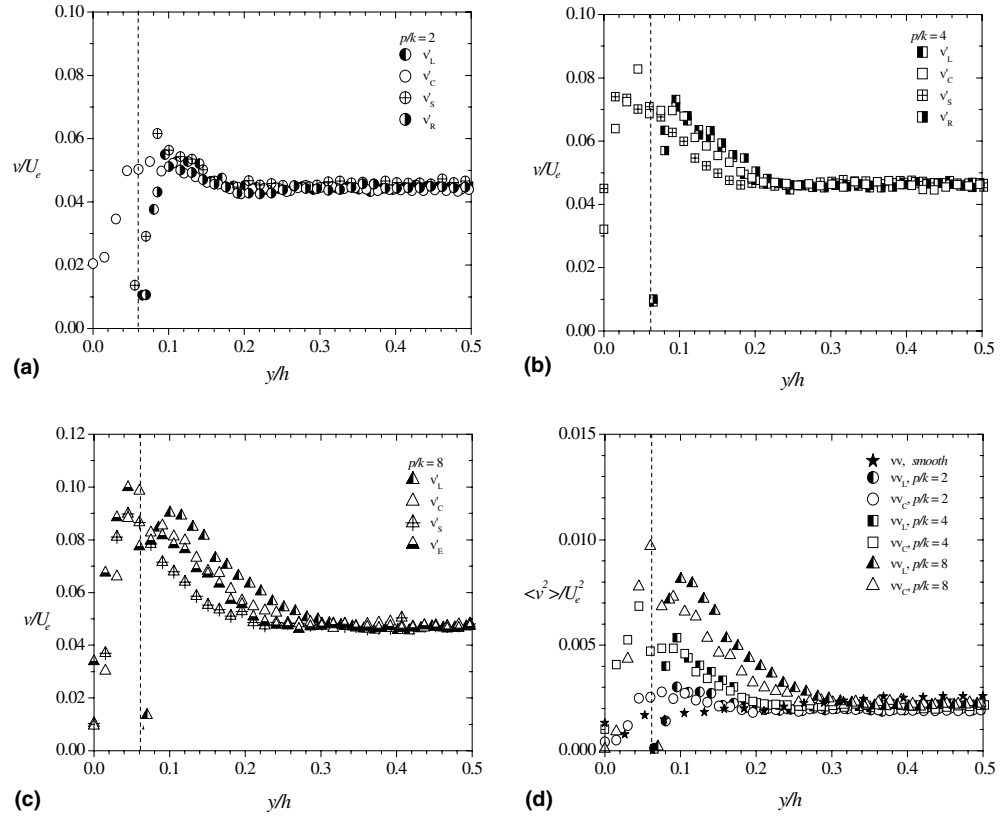

Fig. 10. Wall-normal turbulent intensity (v) and Reynolds stress ($\langle v^2 \rangle$) normalized by freestream velocity (a) d-type, (b) intermediate, (c) k-type and (d) comparison among smooth and various roughness types.

(Fig. 7c) reasonable agreement between profile at cavity center and the other profiles is observed beyond $y/h = 0.2$. The profiles obtained in the cavity and the crests are compared with the upstream boundary layer profile in Fig. 7(d). As expected, U/U_e values for the upstream boundary layer (denoted as *smooth* in Fig. 7(d) and subsequent figures) are higher than those obtained over and between the ribs in the region $y/h < 0.15$. If the roughness sublayer is defined as the region extending from the floor to 5 roughness heights ($y/k < 5$ or $y/h < 0.3$), then Fig. 7 shows that the effects of pitch-to-height ratio or roughness type on the mean flow is limited to the roughness sublayer.

As noted earlier, one effect of surface roughness on the mean flow is to increase the friction coefficient, $C_f = 2(U_\tau/U_e)^2$. Values of the friction velocity for both the smooth and the various roughness types were obtained using the Clauser chart technique, i.e., fitting the mean velocity profiles to the classical log law: $U^+ = \kappa^{-1}\ln y^+ + B - \Delta U^+$; where $U^+ = U/U_\tau$; $y^+ = yU_\tau/\nu$, κ and B are the log-law constants; and ΔU^+ is the roughness function which represents the downward shift associated with roughness in the overlap region. It should be pointed out that the exact values of κ and B have not been calculated in a developing turbulent flow over rough surfaces. However, prior numerical and experimental studies in two-dimensional channels and boundary layers over different types of rough surfaces seem to provide support for universal κ and B values (Cui et al., 2003; Krogstad and Antonia, 1999). In this work, therefore, the following values are used for both the smooth wall and ribs (i.e., rough surfaces): $\kappa = 0.41$ and $B = 5.0$. For a smooth wall, i.e., the upstream boundary layer, $\Delta U^+ = 0$.

Because PIV provides velocity data over finite interrogation areas (and not at points), it is difficult to determine the exact location of the wall. This obviously introduces an error in y and U_τ values, especially for the various roughness types. The exact uncertainty in U_τ could not be obtained but was estimated to be of order 5% and 10% for smooth and ribs, respectively. The mean velocity profiles in inner coordinates are shown in Fig. 8 in a semi-logarithmic format. For each roughness type, profiles for U_C and U_L are shown. For the smooth-wall profile, the data and the log-law overlap up to $y^+ \approx 500$ because of the small wake component compared to a classical zero pressure gradient turbulent boundary layer. Agreement between data and the log-law with the appropriate roughness function is good up to $y^+ \approx 300$ and 400 for the intermediate and k-type roughness, respectively. The values of U_τ and ΔU^+ for the averaged velocity profiles are summarized in Table 1. Fig. 8 and Table 1 clearly show that the roughness shift, ΔU^+, is smallest for d-type roughness and largest for k-type roughness. The skin friction values are higher for the ribs than for the upstream smooth-wall profile because of contribution from pressure-induced drag. It is seen that the pressure induced drag (and hence C_f value) increases with pitch-to-height ratio, as expected.

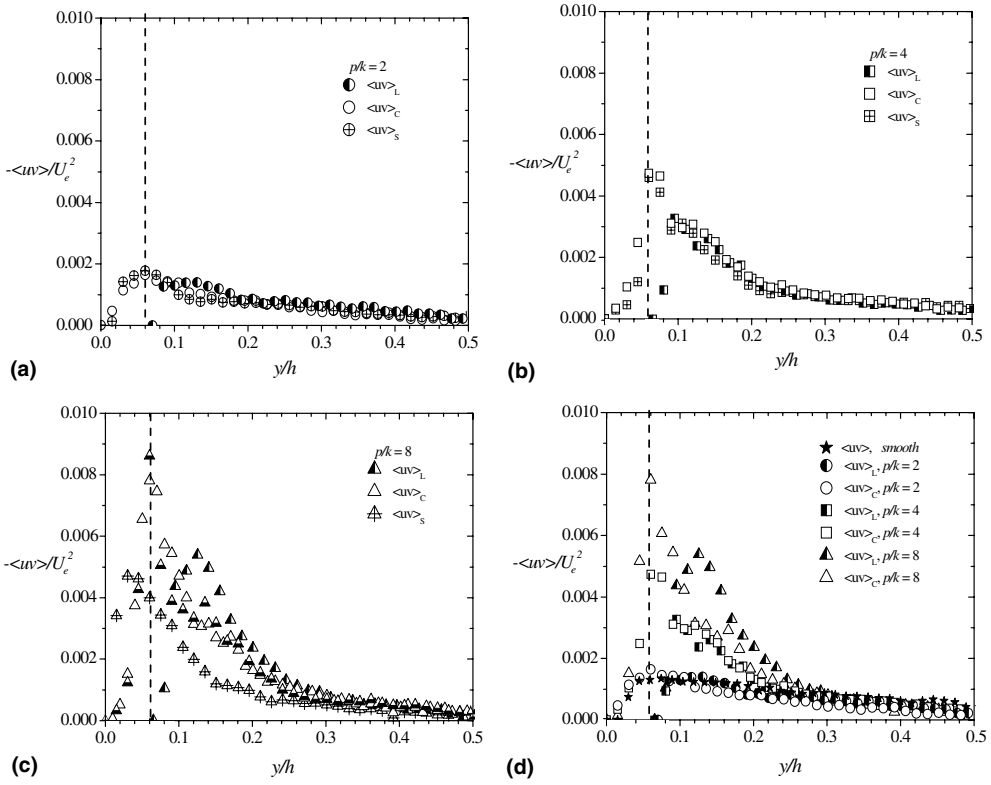

Fig. 11. Reynolds shear stress $-\langle uv\rangle$ normalized by freestream velocity (a) d-type, (b) intermediate, (c) k-type and (d) comparison among smooth and various roughness types.

The values of U_τ/U_e obtained in this work may be compared with values obtained from DNS in channel roughened on one side with circular and square two-dimensional rods (Leonardi et al., 2003) and measurements in a zero pressure gradient turbulent boundary layer over circular rods (Krogstad and Antonia, 1999). Our value of $U_\tau/U_e = 0.062$ for $p/k = 2$ is slightly lower than 0.068 and 0.070 obtained over circular and square rods at the same pitch ratio in the DNS study. For $p/k = 4$ and 8, we obtained $U_\tau/U_e = 0.089$ and 0.105 compared with values of 0.08 and 0.09 obtained for square and circular rods in the DNS study. The value of p/k studied in the boundary layer was 4, and $U_\tau/U_e = 0.057$. The differences between the present and the DNS results are 12% or less, which is comparable to the measurement uncertainty in our U_τ values. Our U_τ/U_e value for $p/k = 4$ is about 60% higher than the value obtained in the boundary layer experiment. The disparity noted above may be due to differences in flow type, rib geometry, Reynolds number and uncertainty in U_τ values.

Prior studies reveal that ribs are effective in augmenting both momentum and heat transfer rates. The rib's effectiveness to increase flow resistance may be quantified by the ratio of the equivalent sand roughness k_s to height, k, of the ribs (k_s/k). In this work, the values of k_s were calculated from the relation: $\Delta U^+ = \kappa^{-1}\ln(k_s^+) + B - C$, where $\kappa = 0.41$, $B = 5.0$ and $C = 8.5$. The dimensionless sand grain roughness, $k_s^+ = k_s U_\tau/\nu$, and k_s/k values are summarized in Table 1. As expected, both k_s^+ and k_s/k are highest for k-type and least for d-type. On basis of k_s^+ values, we found that d-type roughness is in the transitional rough regime while intermediate and k-type are in fully rough regime. Since k_s/k is a measure of the surface to generate resistance to flow, Table 1 indicates that k-type and d-type are, respectively, the most and least effective in generating resistance to flow. The effectiveness of the hemispherical ribs to generate flow resistance can also be compared with other rib geometries. For our intermediate roughness ($p/k = 4$), we obtained $k_s/k = 1.75$. This value is much smaller than $k_s/k = 3.2$ obtained from LES in a channel roughened with square

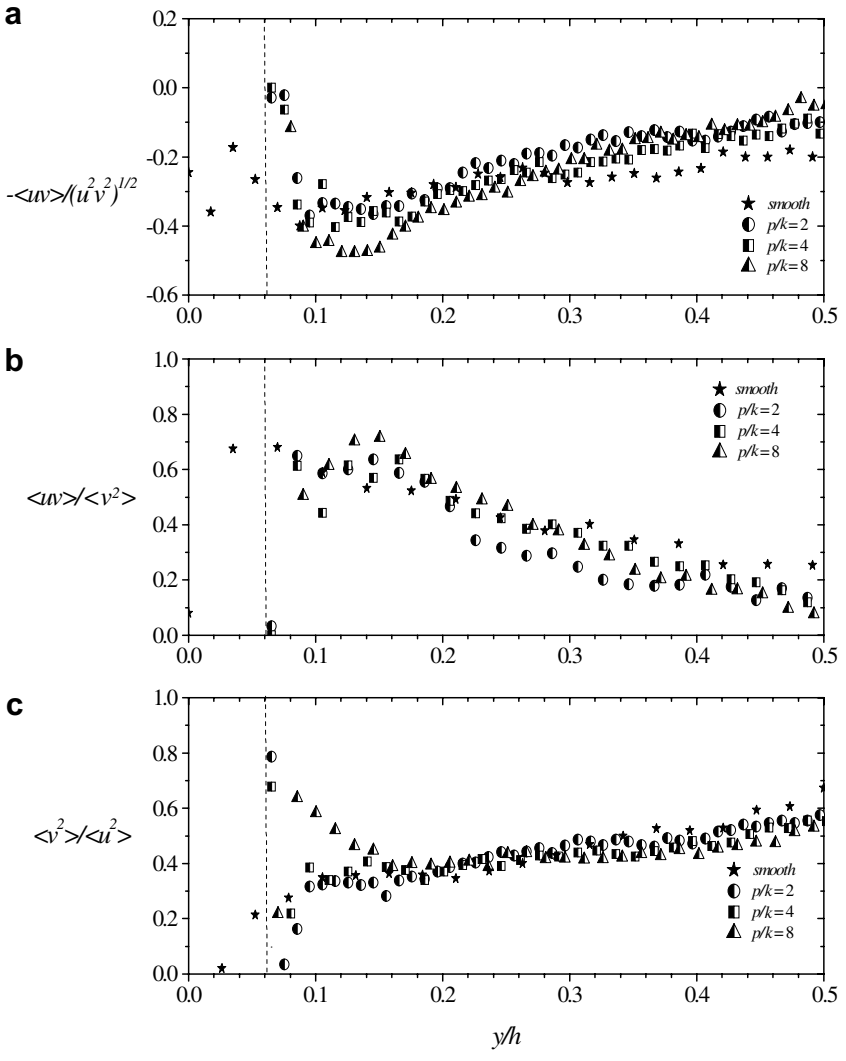

Fig. 12. Distributions of correlation coefficient and stress anisotropy for smooth and various roughness types.

rods, and $k_s/k = 6$ obtained in measurements over circular rods in a zero pressure gradient turbulent boundary layer (Krogstad and Antonia, 1999). For our k-type ($p/k = 8$), $k_s/k = 4.16$ which is also smaller than $k_s/k = 5.9$ obtained in the LES of Cui et al. (2003) in a channel roughened by square rods ($p/k = 9$). It appears, based on this limited comparison, that two-dimensional square and circular rods are more effective in augmenting flow resistance than the hemispherical ribs studied in this work.

3.3. Turbulent intensities and Reynolds shear stress

The turbulence intensity in the streamwise direction, u normalized by the freestream velocity, U_e, is shown in Fig. 9. The various profiles for d-type and intermediate roughness are nearly similar for $y/h > 0.1$. For these roughness types, the peak values obtained at the crests are higher than those obtained in the cavity. For k-type roughness, large differences among the various profiles are observed up to $y/h = 0.25$. This suggests that the region over which the flow is inhomogeneous in the streamwise direction extend further into the outer layer for k-type roughness than noted for d-type and intermediate roughness. Also, in contrast to d-type and intermediate roughness, the peak values for the profiles in the cavity of k-type roughness are higher than corresponding values over the crest. These differences indicate that the interaction between the outer flow and the cavity varies with roughness type or pitch-to-height ratio. It is evident from Fig. 9(d) that the ribs enhance the Reynolds normal stress (u^2) compared to the smooth wall case within the roughness sublayer. The peak values obtained in this study are lower than obtained in previous experiments (Djenidi et al., 1999; Okomato et al., 1993) and LES (Cui et al., 2003) over square ribs. For example, peak values of u obtained in cavity of intermediate and k-type roughness in the present work are 0.14 and 0.17, respectively, and corresponding values for square ribs are 0.20.

The wall-normal component of the turbulence intensity, v, and the Reynolds shear stress, $-\langle uv\rangle$, are shown in Figs. 10 and 11, respectively. Similar to the observations outlined above, v and $-\langle uv\rangle$ profiles obtained over the crest and in the cavity are essentially the same for d-type and intermediate roughness. For k-type, the peak value in the cavity is higher than over the crest. Furthermore, the peak values over and between the ribs are significantly higher than those of the approach boundary layer. The data also show that the turbulence levels are dramatically enhanced as the pitch-to-height ratio increases and the interaction between the shear layers becomes stronger. The peak values of v and $-\langle uv\rangle$ for the hemispheres are lower than in the LES results of Cui et al. (2003) over square ribs, an indication that square rods augment the turbulence intensities and Reynolds shear stress more than hemispherical ribs.

Figs. 9–11 provide evidence that the Reynolds stresses, normalized by the freestream velocity, depend on pitch-to-height ratio in the roughness sublayer. Higher values of the Reynolds stress close to the wall will presumably

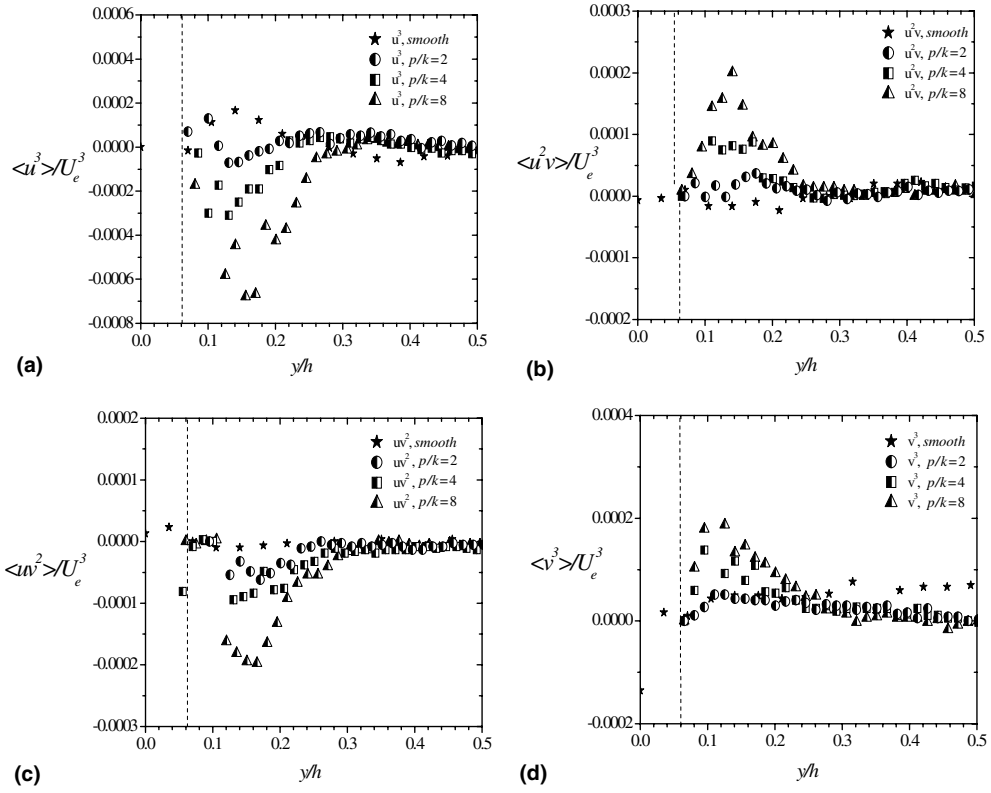

Fig. 13. Triple product normalized by freestream velocity (a) $\langle u^3\rangle$, (b) $\langle u^2v\rangle$, (c) $\langle uv^2\rangle$ and (d) $\langle v^3\rangle$.

lead to enhanced mixing in the vicinity of the ribs. To determine if the increased mixing has any effects on the stress anisotropy and correlation coefficient, we compare values of $R_{uv} = -\langle uv\rangle/\sqrt{u^2v^2}$, $-\langle uv\rangle/v^2$ and v^2/u^2 for three roughness types and smooth surface in Fig. 12. Because of the high background turbulence levels in the outer region of an open channel flow, R_{uv} decreases more rapidly from the wall towards the outer region than reported for channel and boundary layer flows. Close to the wall, $y/h < 0.2$, there are no significant differences among R_{uv} values for smooth, d-type and intermediate roughness. However, the magnitude of R_{uv} is higher for k-type roughness than the other roughness types. Fig. 12(b) shows that $-\langle uv\rangle$ and v^2 are proportionately enhanced by the various roughness types so that the quantity $-\langle uv\rangle/v^2$ remains unchanged from the smooth-wall value. As expected, v^2/u^2 increases away from the wall, an indication that the flow is more isotropic as the free surface is approached. The smooth-wall as well as d-type and intermediate roughness data are fairly low (anisotropic) and similar close to the wall. The flow close to the wall appears more isotropic over k-type roughness as evident in higher v^2/u^2 values (closer to unity) compared to the other surfaces. The various roughness types have no effect on the stress anisotropy in the region $y/h > 0.15$.

3.4. Higher order moments

As is well known, the triple correlations are important turbulent statistics because their gradients represent the turbulent diffusion terms in both the turbulent kinetic energy and Reynolds stress equations. For example, $\langle u^3\rangle$ represents the transport of $\langle u^2\rangle$ by turbulent motion in the streamwise direction, $\langle u^2v\rangle$ and $\langle v^3\rangle$ represent, respectively, the transport of $\langle u^2\rangle$ and $\langle v^2\rangle$ in the wall-normal direction, and $\langle uv^2\rangle$ is associated with 'turbulent work' done by the Reynolds stress. In this work, the following triple products were measured: $\langle u^3\rangle$, $\langle u^2v\rangle$, $\langle uv^2\rangle$ and $\langle v^3\rangle$, and the effects of the various roughness types on these quantities are shown in Fig. 13. Fig. 13(a) and (c) show that $\langle u^3\rangle$ and $\langle uv^2\rangle$ are negative close to the ribs while $\langle u^2v\rangle$ and $\langle v^3\rangle$ (Fig. 13(b) and (d)) are positive. Since $-\partial(\langle u^2v\rangle + \langle v^3\rangle)/\partial y$ is associated with diffusion of

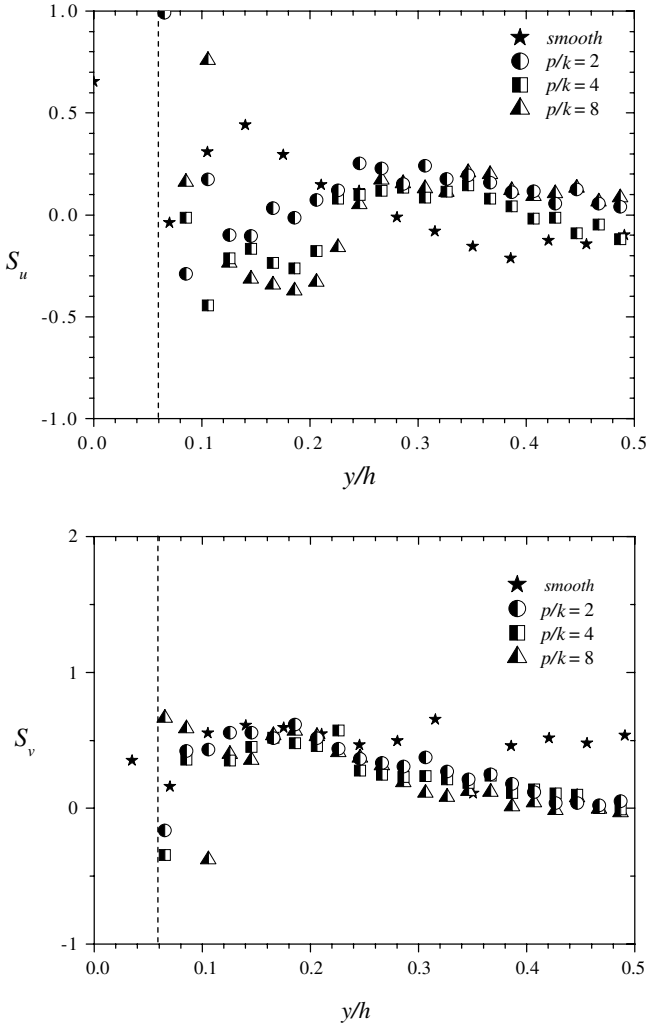

Fig. 14. Skewness factor of fluctuating velocity.

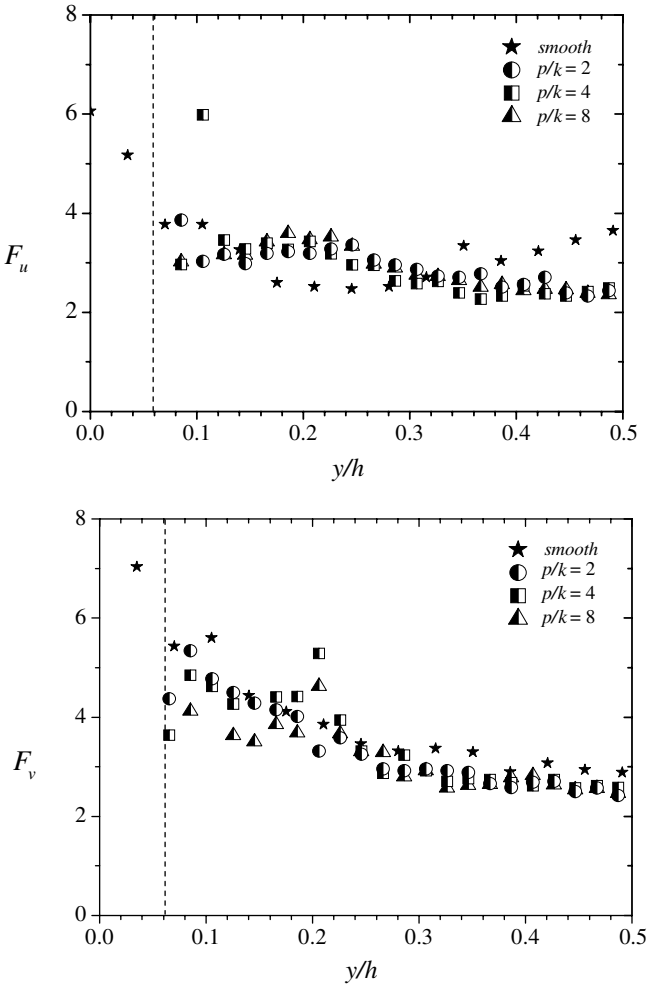

Fig. 15. Flatness factor of fluctuating velocity.

turbulent kinetic energy in the wall-normal direction, it is clear from Fig. 13(b) and (d) that there is negative transport in the region $y/h < 0.15$ and positive transport in the region $0.15 < y/h < 0.2$. Beyond $y/h = 0.2$, there is no significant diffusion of turbulent kinetic energy in the wall-normal direction. Similarly, diffusion of Reynolds shear stress in the wall-normal direction ($\partial\langle uv^2\rangle/\partial y$) is negligible away from the ribs. The magnitude of the triple products is highest for k-type and least for d-type roughness, and this supports previous experiments (Tachie et al., 2003) that turbulent diffusion increases with increasing roughness effects.

The skewness factor ($S_u = \langle u^3\rangle/\langle u^2\rangle^{1.5}$, $S_v = \langle v^3\rangle/\langle v^2\rangle^{1.5}$) and flatness factor ($F_u = \langle u^4\rangle/\langle u^2\rangle^2$, $F_v = \langle v^4\rangle/\langle v^2\rangle^2$) can be used to provide qualitative information on near-wall structure. For example, a nonzero skewness is a signature of acceleration versus deceleration or sweep versus ejection while a flatness factor greater than 3 is normally associated with a peaky signal. The skewness and flatness factors are shown in Figs. 14 and 15, respectively. The negative S_u values close to the ribs may suggest that the instantaneous, U_i, velocity is lower than its mean value, U, more often than not. Since the skewness factor retains sign information, the negative S_u and positive S_v in the region $y/h < 0.2$ indicate that Q4 ($U_i < 0$, $V_i > 0$) events dominate. Similarly, the positive S_u and positive S_v in the region $0.2 < y/h < 0.4$ indicates a dominance of Q1 ($U_i > 0$, $V_i > 0$) events in this region. The flatness factors are fairly close to the Gaussian value of 3 except very close to the ribs which may be due to the presence of large excursion of the fluctuating components of the velocity from their mean values. In general, the skewness and flatness factors do not show any significant sensitivity to differences in roughness type.

3.5. Turbulent kinetic energy budget

The PIV also provides an opportunity to estimate the production and dissipation terms in the turbulent kinetic energy equation. The production and dissipation terms were, respectively, evaluated as follows:

$$\begin{aligned}\text{Prod} &= -\langle u^2\rangle\partial U/\partial x - \langle uv\rangle\partial U/\partial y \\ &\quad - \langle uv\rangle\partial V/\partial x - \langle v^2\rangle\partial V/\partial y\end{aligned}$$

$$\begin{aligned}\varepsilon = -\nu\Bigg[&2\overline{\left(\frac{\partial u}{\partial y}\frac{\partial v}{\partial x}\right)} + \overline{\left(\frac{\partial u}{\partial y}\right)^2} + \overline{\left(\frac{\partial v}{\partial x}\right)^2} \\ &+2\overline{\left(\frac{\partial u}{\partial x}\right)^2} + 2\overline{\left(\frac{\partial v}{\partial y}\right)^2} + 2\overline{\left(\frac{\partial w}{\partial z}\right)^2}\Bigg]\end{aligned}$$

Although the spanwise velocity was not measure, the last term in the dissipation relation was estimated from continuity equation for the fluctuating component as follows: $\overline{(\partial w/\partial z)^2} = \overline{(\partial u/\partial x + \partial v/\partial y)(\partial u/\partial x + \partial v/\partial y)}$. The velocity derivatives were estimated using central differencing. Fig. 16(a) and (b) show distributions of the production and dissipation terms. Both production and dissipation

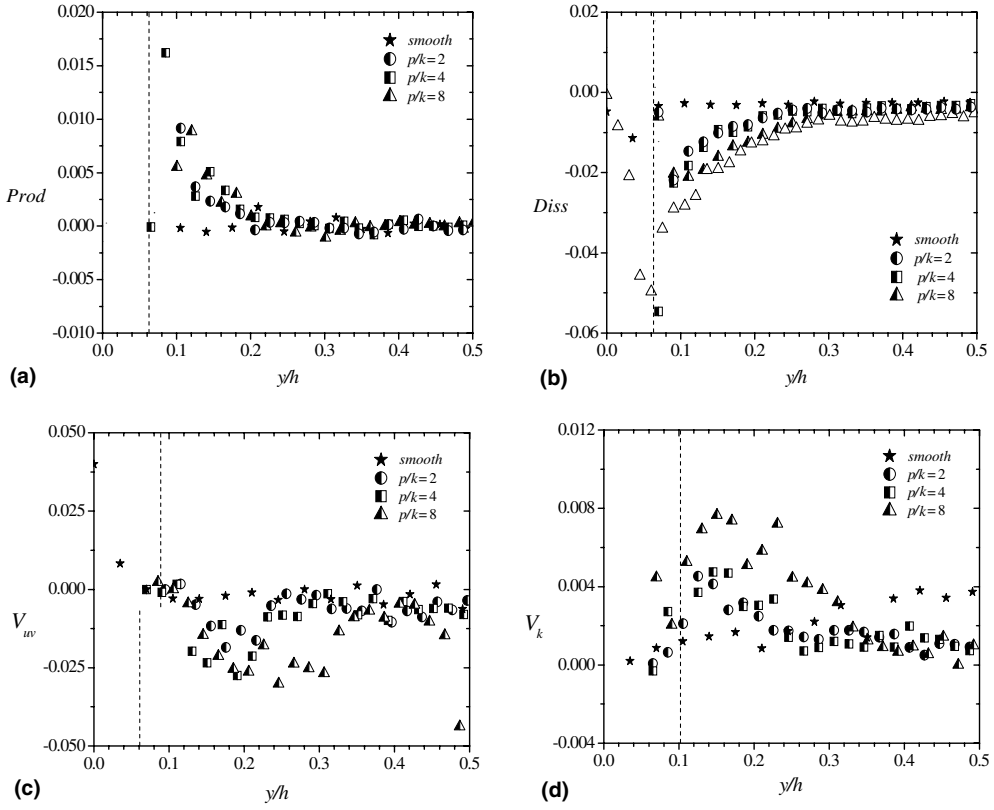

Fig. 16. (a) Production, (b) dissipation, (c) transport velocity of Reynolds shear stress and (d) transport velocity of turbulent kinetic energy.

are nearly zero except close to the ribs, $y/h < 0.2$. The contribution of the various terms in the production term varies with pitch-to-height ratio or roughness type. In all cases, however, $-\langle uv\rangle \partial U/\partial y$ makes the largest contribution to the total production. Since $\partial U/\partial$y and $-\langle uv\rangle$ increase with increasing pitch-to-height ratio, the level of turbulence production increases as roughness effect increases. The dissipation rate of turbulent kinetic energy also increases with increasing pitch-to-height ratio. However, the effects of pitch-to-height ratio on turbulence production and dissipation rate are limited to the roughness sublayer. It is observed that the magnitude of dissipation is higher compared with production close to the ribs (i.e., production $\neq$ dissipation) because the diffusion and convection terms (not shown) are not negligible close to the ribs.

The transport velocities of the turbulent kinetic energy (V_k) and the shear stress (V_{uv}) were also evaluated to see if the different roughness types affect these quantities in any significant manner. The following relations were used to evaluate the transport velocities: $V_k = -k_1(\langle u^2 v\rangle + \langle v^3\rangle)/k_2\ (\langle u^2\rangle + \langle v^2\rangle)$ and $V_{uv} = \langle uv^2\rangle/\langle uv\rangle$, where k_1 and k_2 are approximation constants to account for the contribution of spanwise fluctuating velocity to turbulent diffusion and kinetic energy, respectively. Following prior smooth and rough-wall measurement (e.g., Krogstad and Antonia, 1999) $k_1 = k_2 = 0.75$ was chosen. Fig. 16(c) shows that values of V_{uv} are negative close to the ribs. This supports the notion that Reynolds shear stress is transported from the middle part of the shear layer, where it is mainly produced, inwards to the wall region. Conversely, the positive values of V_k close to the ribs suggest that turbulent kinetic energy is transported from the wall region, where it is mainly produced, outwards to the middle part of the shear layer. The magnitude of the transport velocities is fairly low (V_{uv} is 2.5% or less of freestream velocity; V_k is less than 1% of freestream velocity). It is seen that, similar to the budget terms, the transport velocities increase with increasing roughness effect.

4. Conclusions

The data presented in this work show some important similarities and differences to prior numerical and experimental studies of turbulent flow over two-dimensional square and circular rods. For example, the streamlines for *d*-type, intermediate and *k*-type roughness for the hemispheres studied in this work are qualitatively similar to prior LES and DNS results of Cui et al. (2003) and Leonardi et al. (2003). The mean flow and turbulent quantities vary quite significantly within the cavity as reported in prior works over other geometries, and it appears the outer flow interacts more strongly with *k*-type roughness than *d*-type and intermediate roughness. Compared with two-dimensional square and circular rods, ribs made of hemispheres are less effective in augmenting flow resistance. This is based on the premise that for similar pitch-to-height ratio, the ratio of sand grain roughness to rib height is markedly higher for two-dimensional transverse rods than over the hemispheres. It was also observed that square rods enhance the levels of turbulence than observed in this study. These differences are probably due to the three-dimensional nature of the hemispherical ribs studied in the present work and the specific type of flow (in this case open channel flow).

The results obtained in this study also demonstrate that the ribs effectiveness to augment flow resistance increases with pitch-to-height ratio. Inside the roughness sublayer, the levels of Reynolds stresses, triple products, budget terms in the turbulent kinetic energy equation as well as transport velocities of turbulent kinetic energy and the shear stress increase with increasing pitch-to-height ratio. This is explained by a more enhanced interaction between the cavity and outer flow as the pitch-to-height ratio increases. While the stress anisotropy for *d*-type and intermediate roughness remains similar to smooth data close to the wall, we found a strong tendency towards isotropy for *k*-type roughness.

Acknowledgements

The second author gratefully acknowledges financial support provided by Canada Foundation for Innovation, Manitoba Hydro and Natural Sciences and Engineering Research Council of Canada. Mr. Shashidar Makkapati helped in data processing.

References

Akinlade, O.G., Bergstrom, D.J., Tachie, M.F., Castillo, L., 2004. Outer flow scaling of smooth and rough wall turbulent boundary layers. Expt. Fluids 3 (4), 604–612.

Alireza, A., Anderson, H.I., Manhart, M., 2004. DNS of turbulent flow in a rod-roughened channel. Int. J. Heat Fluid Flow 25, 373–383.

Cui, J., Patel, V.C., Lin, C.-L., 2003. Large-eddy simulation of turbulent flow in a channel with rib roughness. Int J. Heat Fluid Flow 24, 372–388.

Djenidi, R., Elavaransan, R., Antonia, R.A., 1999. The turbulent boundary layer over transverse square cavities. J. Fluid Mech. 395, 271–294.

Furuya, Y., Miyata, M., Fujita, H., 1976. Turbulent boundary layer and flow resistance on plates roughted by wires. ASME J. Fluids 9, 2429–2442.

Grass, A.J., Stuart, R.J., Mansour-Tehrani, M., 1993. Common vortical structure of turbulent flows over smooth and rough boundaries. AIAA J. 31, 837–847.

Ikeda, T., Durbin, P.A., 2002. Direct numerical simulation of a rough wall channel flow. Report No. TF-81, Flow Physics and Computation Division, Department of Mechanical Engineering, Stanford University, Stanford, CA, USA.

Jiménez, Javier., 2004. Turbulent flows over rough walls. Ann. Rev. Fluid Mech. 36, 173–196.

Krogstad, P.-Å., Antonia, R.A., 1999. Surface roughness effects in turbulent boundary layers. Exp. Fluids 27, 450–460.

Krogstad, P.-Å., Antonia, R.A., Browne, L.W.B., 1992. Comparison between rough- and smooth-wall turbulent boundary layers. J. Fluid Mech. 245, 599–617.

Krogstad, P.-Å., Andersson, H.I., Bakken, O.M., Ashrafian, A., 2005. An experimental and numerical study of channel flow with rouge walls. J. Fluid Mech. 530, 327–352.

Leonardi, S., Orlandi, P., Djenidi, L., Antonia, R.A., 2003. Direct numerical simulations of turbulent channel flow with transverse square bars on one wall. J. Fluid Mech. 491, 229–238.

Leonardi, S., Orlandi, P., Antonia, R.A., 2005. A method for determining the frictional velocity in a turbulent channel floor with roughness on one wall. Exp. Fluids 3 (6), 796–800.

Ligrani, P.M., Moffat, R.J., 1986. Structure of transitionally rough and fully rough turbulent boundary layers. J. Fluid Mech. 162, 69–98.

Liou, T.-M., Chang, Y., Hwang, D.-W., 1990. Experimental and computational study of turbulent flows in a channel with two pairs of turbulence promoters in tandem. Trans. ASME 112, 302–310.

Mazouz, A., Labraga, L., Tournier, C., 1998. Anisotropy invariants of Reynolds stress tensor in a duct flow and turbulent boundary layer. Trans. ASME 120, 280–284.

Miyake, Y., Tsujimoto, K., Agata, Y., 2001. Direct numerical simulation of rough wall heat transfer in a turbulent channel flow. Int. J. Heat Fluid Flow 22, 237–244.

Nagano, Y., Hattori, H., Yasui, S., Houra, T., 2003. DNS of velocity and thermal fields in turbulent channel flow with transverse-rib roughness. In: Kasagi, N., Eaton, J.K., Friedrich, R., Humphrey, J.A.C., Leschziner, M.A., Miyauchi, T. (Eds.), Proceedings of the Third International Symposium on Turbulence and Shear Flow Phenomena, pp. 1055–1060.

Nikuradse, J., 1933. Strömungsgesetze in Rauhen Rohren, VDI-Forsch. 361 (Engl. Transl. 1950. Laws of flow in rough pipes. NACA TM 1292).

Okomato, S., Seo, S., Nakaso, K., Kawai, I., 1993. Turbulent shear flow and heat transfer over the repeated two dimensional square ribs on ground plane. J. Fluids Eng. 115, 631–637.

Perry, A.E., Schofield, W.H., Joubert, P.N., 1969. Rough wall turbulent boundary layers. J. Fluid Mech. 37, 383–413.

Raupach, M.R., Antonia, R.A., Rajagopaplan, S., 1991. Rough-wall turbulent boundary layers. Appl. Mech. Rev. 44, 1–25.

Sato, H., Hishida, K., Maeda, M., 1989. Turbulent flow characteristics in a rectangular channel with repeated rib roughness. In: Heat Transfer in Convective Flows, National Heat Conference HTD 107, pp. 191–196.

Tachie, M.F., Bergstrom, R., Balachandar, D.J., 2003. Roughness effects in low-Re_θ open channel turbulent boundary layers. Exp. Fluids 35, 338–346.